AVS Quantum Science

RESEARCH ARTICLE | OCTOBER 25 2024

All-in-one quantum diamond microscope for sensor characterization FREE

Connor Roncaioli ; Connor A. Hart ; Ronald Walsworth ; Donald P. Fahey

Check for updates

AVS Quantum Sci. 6, 044403 (2024)
https://doi.org/10.1116/5.0222809

View Online
Export Citation

Articles You May Be Interested In

Communicating the science of climate change
Physics Today (October 2011)

The curious aftermath of Neptune's discovery
Physics Today (December 2011)

Roaming reactions: The third way
Physics Today (November 2011)

25 October 2024 16:33:38

AVS
AIP Publishing



All-in-one quantum diamond microscope for sensor characterization

Cite as: AVS Quantum Sci. **6**, 044403 (2024); doi: 10.1116/5.0222809
Submitted: 10 June 2024 · Accepted: 9 October 2024 ·
Published Online: 25 October 2024

View Online Export Citation CrossMark

Connor Roncaioli,[1,2,a] Connor A. Hart,[2] Ronald Walsworth,[2] and Donald P. Fahey[1,2]

AFFILIATIONS

[1]DEVCOM Army Research Laboratory, Adelphi, Maryland 20783-1138, USA
[2]Quantum Technology Center, University of Maryland, College Park, Maryland 20742, USA

[a)]Electronic mail: connor.a.roncaioli.civ@army.mil

ABSTRACT

Ensembles of nitrogen-vacancy (NV) centers in diamond are a leading platform for sensing and imaging magnetic fields at room temperature, in part due to advances in diamond growth. An essential step to improving diamond material involves the characterization of crystal and NV-related properties, such as strain and paramagnetic impurities, which can shift and broaden the NV resonances used for sensing. Full sample characterization through wide-field imaging enables both fast and detailed feedback for growers, along with the estimation of sensing performance before use. We present a quantum diamond microscope tailored for millimeter-scale wide-field mapping of key quantum properties of NV-diamond chips, including NV ensemble photoluminescence intensity, spin-lattice relaxation time (T_1), and spin-coherence lifetimes (T_2 and T_2^*). Our design also allows for lattice stress/strain and birefringence magnitude/angle mapping, and their *in situ* correlation with NV properties.

Published by AIP Publishing. https://doi.org/10.1116/5.0222809

25 October 2024 16:33:38

I. INTRODUCTION

Solid state quantum sensors, such as the nitrogen-vacancy (NV) center in diamond, are undergoing rapid research and commercial expansion. NV-diamond sensing modalities include scalar[1–6] and vector[7,8] magnetic field sensing and imaging, stable clock oscillators,[9,10] electric field sensors,[11,12] nanodiamond temperature sensors,[6,13] mapping of strain in the diamond crystal,[14,15] microwave mode cooling,[16,17] extreme environment magnetometry,[18] and pressure sensing.[19] The rise in NV sensors has been aided by advances in diamond growth and a better understanding of fabrication properties and their relation to performance.[20]

A widely used instrument is the quantum diamond microscope (QDM), which employs a dense layer of NV centers (≈ few micrometer) on a millimeter-scale diamond plate to perform wide-field micrometer-scale vector imaging of magnetic fields at very low standoff distances.[21,22] These measurements benefit from low-strain diamond chips with narrow linewidth NV center resonances. Prior characterization of the diamond also aids in identifying artifacts that play an outsized role in some instances,[23–25] as well as imperfections that limit QDM performance.[14,26,27] Developers of quantum diamond require a tool that is sensitive to the NV spin and strain environment, especially on samples that are too thin for optical absorption measurements. Here, we demonstrate an "all-in-one" QDM that can image several parameters relevant to NV ensemble sensing across a millimeter diamond plate, including NV spin resonance line shift, decoherence, depolarization time scales, stress/strain, and birefringence. Measurements are co-registered to simplify analysis of complex features that appear across modalities.

II. INSTRUMENT OVERVIEW

The all-in-one QDM is configurable between multiple measurement modalities, as listed in Table I. A high-level depiction of the apparatus is illustrated in Fig. 1 and the supplementary material includes a summary of each measurement modality and list of components for each subsystem.

Laser light for NV excitation can be sent through a top objective for point-excitation or to a periscope that illuminates a millimeter-scale region of the diamond along a shallow angle. Similarly, there are two collection pathways for NV photoluminescence (PL); the top objective can be used to collect epifluorescence and spatially filter it before being sent to either a photodiode for time resolved confocal measurement or a fiber-coupled spectrometer for spectroscopy; or the PL can be collected by an imaging objective mounted beneath the sample space, which directs light to a camera for wide-field imaging. This combination is powerful in that it automatically correlates confocal and imaged NV measurements, which enhances analysis.

TABLE I. All-in-one QDM measurement modalities: CLE—confocal laser excitation using epifluorescent illumination, FSLE—full sample laser excitation, LED—light-emitting diode, PD—photodiode, CMOS—complementary metal–oxide semiconductor camera.

	Measurement details		
Measurement	Pump geometry	Read-out configuration	Purpose
Constant wave-optically detected magnetic resonance (CW-ODMR)	CLE	PD	MW resonance frequencies of NV spin transitions
Rabi	CLE	PD	MW driving rate of NV spins
T_1 relaxometry	CLE	PD	NV spin-lattice relaxation time (T_1)
Ramsey	CLE	PD	NV spin dephasing time (T_2^*)
Hahn echo	CLE	PD	NV spin decoherence time (T_2)
Dynamic decoupling	CLE	PD	Performance of noise-cancelling pulse sequences outside of specified frequency window
Photoluminescence (PL) distribution	FSLE or CLE	CMOS	NV PL intensity and epi-spot location[a]
Imaged CW-ODMR	FSLE	CMOS	NV spin resonance across sample
Imaged Rabi	FSLE	CMOS	MW driving rate of NVs across sample
Imaged T_1 relaxometry	FSLE	CMOS	NV T_1 across sample
Imaged Ramsey	FSLE	CMOS	NV T_2^* across sample
Imaged Hahn echo	FSLE	CMOS	NV T_2 across sample
Imaged dynamic decoupling	FSLE	CMOS	Performance of noise-cancelling pulse sequences across sample
	Illumination source		
Imaged quantitative birefringence	LED	CMOS	Spatial distribution of stress/strain within diamond plate

[a]A supplement to photodiode measurements, showing the precise location of the pump spot relative to the sample in imaged measurements.

Furthermore, a sliding mount exchanges the top objective with an LED-polarizer pair, enabling birefringence transmission measurements detailed in Sec. III C.

The system is capable of strong microwave driving of NV spin transitions (>MHz Rabi frequency) across the full field of view of the imaging objective (≈ 5 mm), enabling wide-field imaging of pulsed diagnostics (e.g., Ramsey, Hahn echo). An NV Rabi frequency similar to $1/T_2^*$ across the entire diamond is necessary to achieve multiple Rabi periods before dephasing occurs. Large, uniform microwave intensities are achieved by way of a metallic loop gap resonator (LGR) adapted from a previous work.[28] The resonator design greatly enhances the microwave field while having sufficient bandwidth to collect optically detected magnetic resonance (ODMR) spectra up to a few-millitesla bias magnetic fields. Details are provided in the supplementary material.

A megapixel camera images a millimeter-scale field-of-view with micrometer resolution resulting in over $\times 10^6$ spectral datasets. Fitting the datasets to produce spatially resolved parameter maps is massively sped up through the use of parallel GPU-based fitting software, such as GPUfit and the associated python-based pyGPUfit module.[29] For CW-ODMR, Rabi, and T_1 relaxometry, measurements are reported as contrast: $C = I_{\mathrm{MWon}}/I_{\mathrm{MWoff}}$. Here, I_{MWon} is the measured PL signal intensity with microwaves on, and I_{MWoff} is the reference PL intensity measurement with microwaves off. For phase-sensitive modalities (Ramsey and Hahn echo), values are reported as a visibility $V = (I_{\mathrm{MW+}} - I_{\mathrm{MW-}})/(I_{\mathrm{MW+}} + I_{\mathrm{MW-}})$. Here, $I_{\mathrm{MW+}}$ is the measured PL intensity where all microwave pulses applied to the NVs have the same phase, and $I_{\mathrm{MW-}}$ is PL intensity with the final $\pi/2$ microwave pulse of opposite phase. More details, such as the functional form of the various fit procedures and techniques for evaluating fit appropriateness are provided in the supplementary material.

III. EXPERIMENTAL MODALITIES

A. CW-ODMR

Continuous (CW)-ODMR spectroscopy provides a wealth of knowledge. By separating the NV classes with a uniform magnetic bias field and fitting the NV resonances to find their center frequencies, several quantities can be measured including local magnetic field, temperature, and crystal stress/strain. Confocal CW-ODMR through the top objective is used when precise control of the sensing volume or maximum sensitivity is required. Imaged CW-ODMR, performed via full sample side illumination and imaged onto the megapixel camera, allows measurement of the NV spin resonance spectrum on a pixel-by-pixel basis. CW-ODMR is commonly used to image magnetic fields; an example is provided in the supplementary material.

25 October 2024 16:33:38

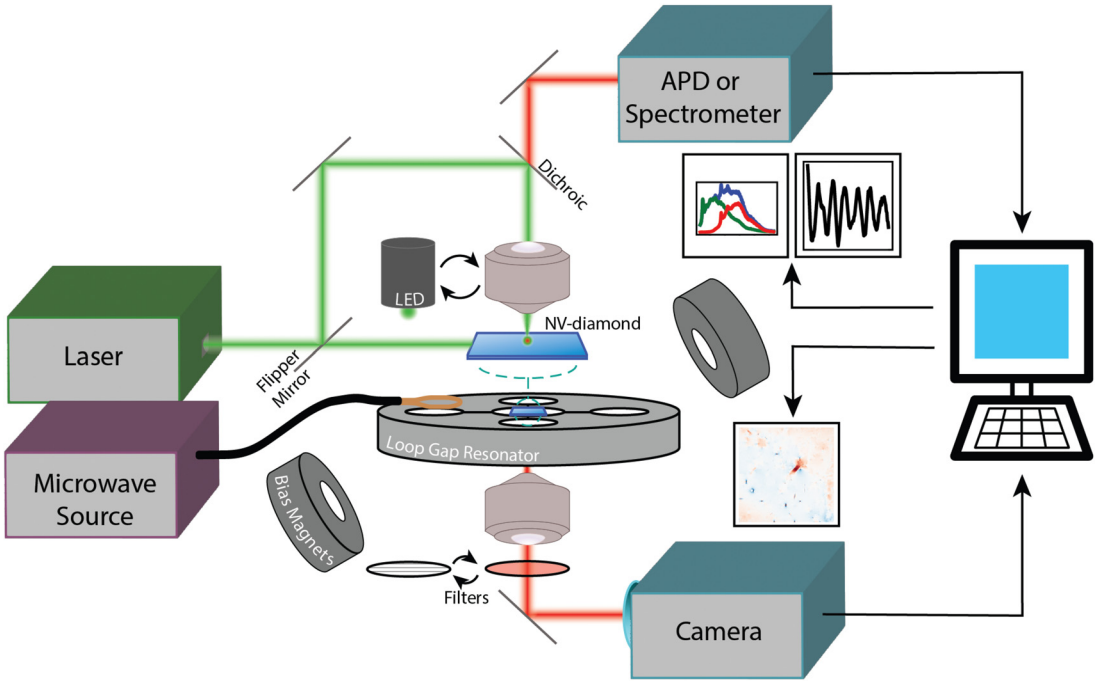


FIG. 1. Schematic of all-in-one QDM for NV-diamond sensor characterization. Two optical excitation pathways are exchanged by use of a flipper mirror, with an epifluorescent option and a non-focused full sample excitation option. Microwaves are coupled in to an edge inductive gap of the loop gap resonator (LGR), creating a strong, homogeneous microwave field across the full NV-diamond sample. Permanent magnets create a uniform bias magnetic field that Zeeman shifts NV spin resonances in order to isolate or overlap resonance frequencies as needed. Optical objectives above and below the sample are used for epifluorescent or full field-of-view measurements. The avalanche photodiode (APD) and optical spectrometer are coupled to the above-mentioned sample collection pathway. The APD is used for time-resolved NV photoluminescence (PL) measurements, while the spectrometer is used for microwave assisted NV charge state measurements. The below-sample objective is coupled to a long-pass filter and camera used to image PL for spatially resolved NV characterization. An LED with linear polarization control and appropriate circular polarization filter can be switched for the top objective and bottom filters, respectively, to create a transmission measurement of optical birefringence using the same below-sample objective and camera.

This modality can map interactions that affect the NV spin Hamiltonian, including crystal stress and strain. Based on previous work,[14,15] we describe the NV stress tensor,

$$\sigma_{\mathrm{Diag}} = \frac{1}{4a_1}[M_{z,1} + M_{z,2} + M_{z,3} + M_{z,4}], \quad (1)$$

$$\sigma_{XY} = \frac{1}{8a_2}[M_{z,1} + M_{z,2} - M_{z,3} - M_{z,4}], \quad (2)$$

$$\sigma_{XZ} = \frac{1}{8a_2}[M_{z,1} - M_{z,2} + M_{z,3} - M_{z,4}], \quad (3)$$

$$\sigma_{YZ} = \frac{1}{8a_2}[M_{z,1} - M_{z,2} - M_{z,3} + M_{z,4}], \quad (4)$$

where $\sigma_{\mathrm{Diag}} = \sigma_{XX} + \sigma_{YY} + \sigma_{ZZ}$ is the diagonal stress tensor component, the individual values of which are obscured in present QDM measurements; $M_{z,i}$ are the asymmetric line shift values for each NV orientation classes within the diamond crystal about their mean value; and $\{a_1, a_2\} = \{4.86, -3.7\}$ MHz/GHz is the spin–stress coupling constant. Using these relationships, we can partially reconstruct the stress tensor, including the shear components, from QDM measurements (see the supplementary material). Note that determination of the individual uniaxial terms (σ_{XX}, etc.) is possible by changing the bias magnetic field direction, though we have not implemented it here.[14]

B. Pulsed protocols

Pulsed NV measurements are performed in either the confocal or wide-field imaging modes, including protocols for Rabi oscillation, Ramsey, Hahn echo, and T_1 relaxometry, see Figs. 3 and 4. Importantly, the all-in-one QDM allows such measurements over a millimeter-scale field-of-view—whereas past measurements were limited to $\approx 100\,\mu$m[21]—due to integration of the LGR to provide strong, homogeneous microwave driving of NV spin transitions.

Imaging the NV Rabi frequency allows evaluation of microwave field homogeneity. Ramsey and Hahn echo measurements are used to evaluate the NV ensemble spin dephasing time T_2^* and are conducted at a fixed microwave detuning (≈ 5 MHz) from the NV center frequency in order to have sufficiently fast oscillation to properly fit the decay envelope. Hahn echo measurements are used to measure the NV ensemble decoherence time T_2. Both Ramsey and Hahn echo measurements are collected with phase dependence of the final microwave pulse in order to measure visibility instead of contrast for improved noise cancelation. Finally, T_1 relaxometry provides an upper limit to NV spin lifetimes in the sample. Dynamical decoupling schemes are feasible for this system but are not implemented in the present work. Examples of imaged fitting parameters extracted from these measurements are provided in Figs. 4 and 5. Correlation is observed between high-contrast features in the maps of stress and T_2^*, which is consistent with past studies of CW-ODMR and Ramsey microscopy of NV-

25 October 2024 16:33:38

diamond samples.[26] However, the T_2 and T_1 maps are largely homogeneous, as anticipated for the high-quality NV-diamond sample studied here. More detail is provided in Sec. IV.

C. Optical birefringence and stress imaging

The cubic symmetry of ideal diamond has zero optical birefringence; however, real diamond samples typically have local stress that breaks this symmetry, resulting in observable birefringence.[30] The all-in-one QDM provides a quantitative measure of stress in the diamond sample via a switchable stage that brings an LED ($\lambda = 530$ nm) with a rotating linear polarizer above the diamond sample and a circular analyzer after the below-sample objective. In this operational mode, optical transmission measurements yield the full 2D anisotropic retardance vector without adjusting the sample.[14] The stress angle ϕ and retardance phase $\delta = (2\pi/\lambda)\Delta n L$, where L is the sample thickness and Δn is the difference in refractive index between the two polarizations, are related to the optical transmission intensity by the following equation:

$$I_i = \frac{1}{2} I_0 [1 + \sin(2(\alpha_i - \phi)) \sin(\delta)]. \quad (5)$$

By measuring I_i as the linear polarizer angle, α_i rotates through 180°, and ϕ and sin δ are determined. δ is related to the optical wavelength λ, the diamond stress magnitude ($|\sigma|$), and the index of refraction $n = 2.42$ by the following equation:

$$|\sigma| \approx \frac{2}{3\pi} \frac{|\delta|\lambda}{L n^3 q_{iso}}, \quad (6)$$

where $q_{iso} = 0.3 \times 10^{-12} \text{Pa}^{-1}$ is a piezo-optical coefficient.[31]

Stress determined in this way may be buried deep in the undoped diamond, far away from the active layer of NVs. Additionally, small regions of intense stress in the NV layer may not be detectable by birefringence against the contribution of a large undoped diamond, if the active layer is comparatively small. Furthermore, if the diamond has significant strain or the sample is of sufficient thickness, the optical birefringence measurement can become phase-ambiguous once the difference between the slow and fast axes $|\delta| \geq (\lambda/2)$. These are all reasons that multi-modal detection is crucial for complete characterization of NV samples. Comparison of measurements of stress determined by CW-ODMR (contribution confined to the NV layer) to optical birefringence (contribution from the entire diamond) are presented in Figs. 4(a), 4(e), and 4(f).

D. Optical spectroscopy and NV charge state characterization

Top-collected PL may be sent to a spectrometer via a flip mirror and analyzed for NV charge state ratio or the presence of other color centers. We have found that a fiber-coupled compact CCD spectrometer is sufficient for most ensemble measurements.

Two NV charge states are present in most samples, NV^- and NV^0, but only NV^- is useful for sensing. In quantum-grade diamond growth, it is common to try to maximize the amount of nitrogen converted to NV^-. We determine the ratio of NV^- to NV^0 by collecting PL spectra with and without a microwave field resonant with the NV^- spin transitions, which allows for their decomposition.[32]

NV charge states are metastable and dependent on both intrinsic material and extrinsic experimental conditions. Intrinsic conditions that can affect the NV charge state include local availability of electron donors by doping[33] and local chemical potential.[34] Some samples can have coexisting regions of different charge state ratios.[35] Extrinsic conditions that can affect the NV charge state include electric field bias,[36,37] laser intensity,[38] and excitation wavelength.[39] NV^- fraction as a function of laser intensity is particularly important to characterize since it falls off at high intensities, which needs to be balanced against NV PL for optimal sensing.[22]

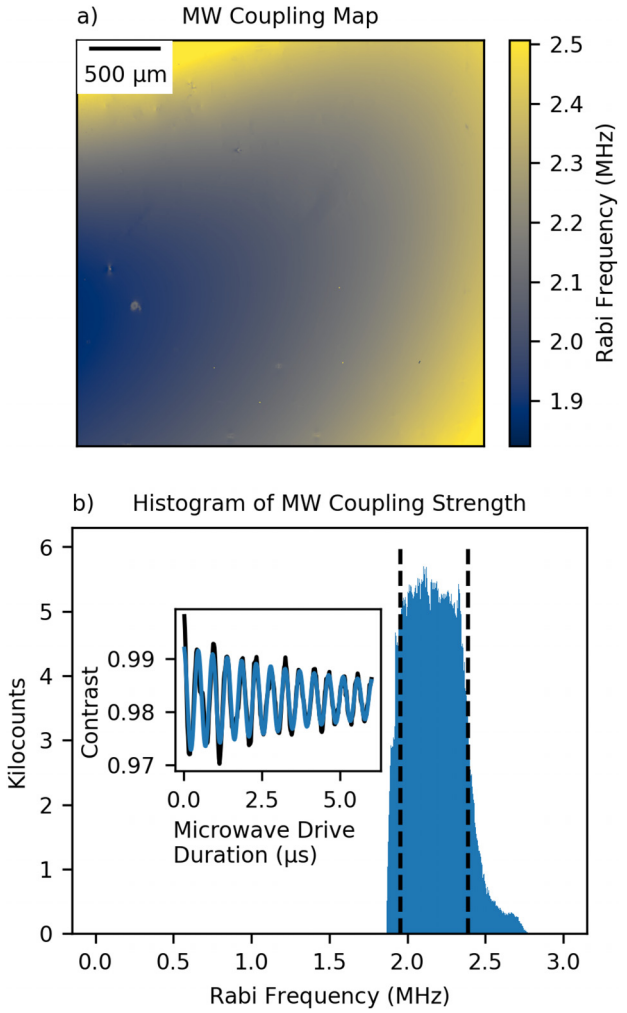


FIG. 2. (a) Example map of NV ensemble Rabi frequency produced by all-in-one QDM across $\approx 3 \times 3\,\text{mm}^2$ region of a diamond sensor plate. NV-diamond sample is described in Sec. IV. Observed variation in Rabi frequency across field-of-view results from spatial gradients in microwave coupling strength to NV spin transitions, e.g., due to inhomogeneous microwave drive amplitude or angle of incidence relative to the interrogated NV dipole, or any cause of NV spin resonance line shift or broadening. Spatial scale bar is shown. (b) Histogram of fit values provides an estimate of Rabi frequency distribution across all-in-one QDM field-of-view. 10th and 90th percentiles, marked with dashed black lines, fall within ± 10% of mean Rabi frequency value. Inset: example single pixel Rabi oscillation dataset and associated fit in blue.

25 October 2024 16:33:38

IV. DIAMOND CASE STUDY

As a demonstration of the all-in-one QDM, we characterize a quantum-grade NV-diamond sample produced by Element Six. This sample is $3 \times 3 \times 0.5\,\mathrm{mm}^3$ of diamond host grown by chemical vapor deposition (CVD), with a $20\,\mu\mathrm{m}$ thick layer (16 ppm N, 3 ppm NV) adjacent to the as-grown surface. With this geometry, well above 99% of the NV defects are >100 nm below the surface, and are not sensitive to surface effects. Additionally, we do not anticipate the existence of ferromagnetic or paramagnetic inclusions in this CVD grown sample. A similar diamond is used in previous work to achieve volume-normalized DC magnetic field sensitivity of $\eta^V = 34\,\mathrm{nTHz}^{-1/2}\,\mu\mathrm{m}^{3/2}$.[40]

The sample is treated with a tri-acid perchlorate solution[41] in order to remove surface contaminants and characterized by XPS to discern surface composition; additional details are provided in the supplementary material. The sample is then characterized with the

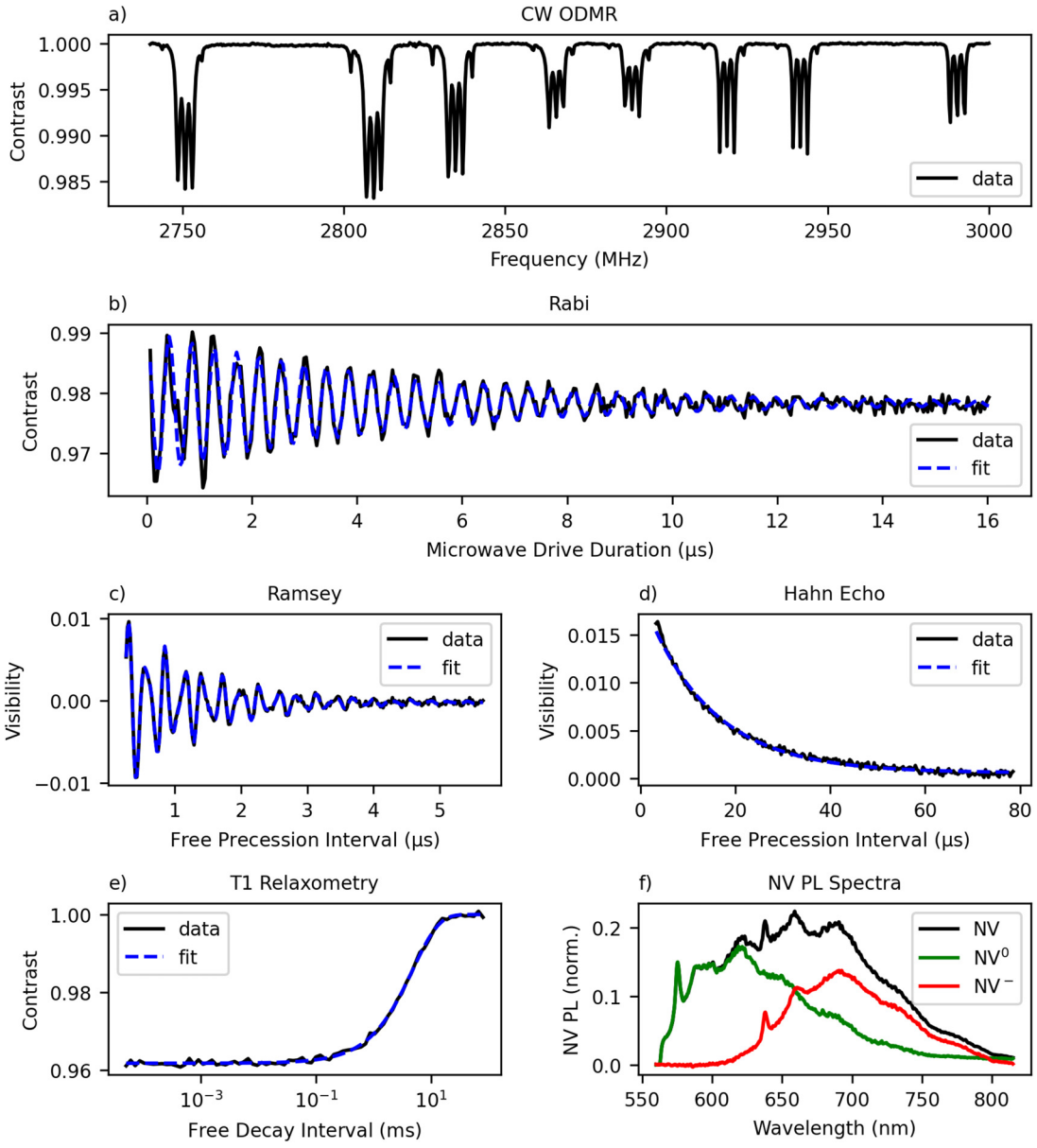


FIG. 3. Example NV ensemble measurements for diamond sample described in Sec. IV, and associated fits for data, collected with the all-in-one QDM in the epifluorescence configuration. (a) CW-ODMR spectra; (b) Rabi oscillation; (c) Ramsey measurement; (d) Hahn echo; (e) T_1 relaxation; and (f) NV PL spectra demonstrating MW-assisted charge state decomposition as described in Ref. 30. For the CW-ODMR data, LGR resonant frequency ≈ 2785 MHz and a bandwidth ≈ 80 MHz, which enhances MW driving of nearby resonant NV spectral features arising from different projections of bias magnetic field on four NV orientations within the diamond crystal.

25 October 2024 16:33:38

all-in-one QDM, performing both confocal and imaged CW-ODMR, Rabi, Ramsey, and Hahn echo, as well as imaged optical birefringence of the entire sample, imaged stress of the NV layer, and confocal microwave-assisted spectroscopy to determine relative NV charge states (see Figs. 2–5). After alignment, the diamond sample remains untouched until all measurements are completed, so that imaged modalities are co-registered to within one pixel, enabling precise correlation of features between measurements.

For the wide-field imaging modalities, significant heating of the diamond sample is caused by laser illumination at typical input power of a few watts. Heating leads to an asymmetric line shift of NV spin resonances, which can result in a line shift gradient across the sample.

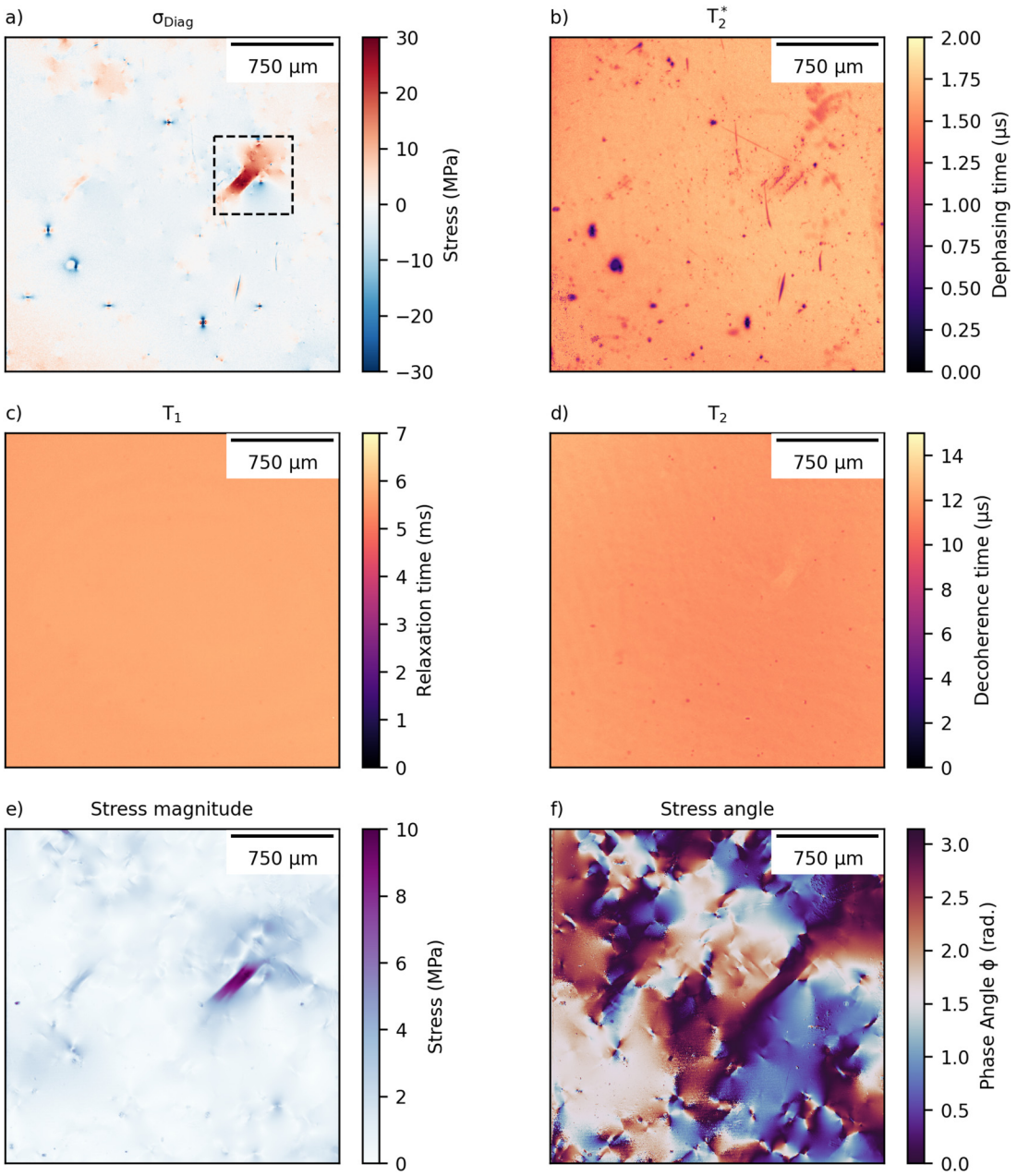


Fig 4. Example of NV-diamond sample characterization performed with all-in-one QDM and displayed as image data. (a) σ_{Diag} extracted from CW-ODMR; (b) T_2^* from Ramsey; (c) T_1 from relaxometry; (d) T_2 from Hahn echo; (e) stress magnitude, and (f) stress angle determined from optical birefringence. Correlations in (a)–(f) relate to regions of high stress and stress gradients. A discussion of sources of noise and error in these and related measurements is provided in the supplementary material.

25 October 2024 16:33:38

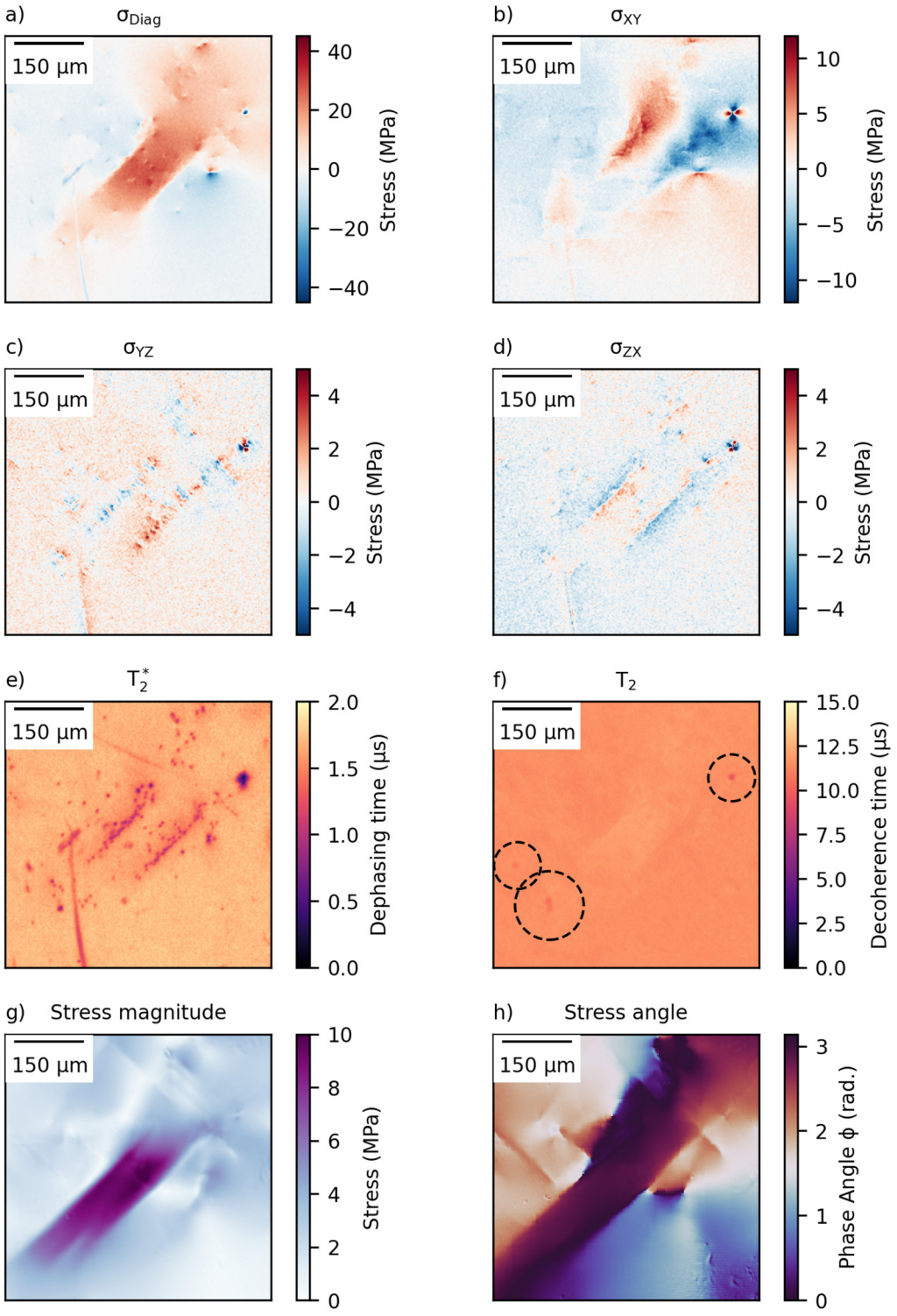


Fig 5. Expanded-view QDM characterization images for the region of NV-diamond sample indicated by box in Fig. 4(a): this region of enhanced stress appears as a channel between two highly localized linear regions. (a) Diagonal stress tensor component σ_{Diag} extracted from CW-ODMR corresponds to isometric stress. (b)–(d) Off diagonal stress tensor components correspond to shear stress, with σ_{XY} being in-plane shear and σ_{YZ} and σ_{ZX} being out-of-plane shear components. (e) T_2^* map shows qualitative correlation with stress measurements. (f) T_2 map is near-uniform with the exception of a few marked regions degraded by poor T_2^*. (g) Stress magnitude and (h) stress angle determined from optical birefringence measurements.

25 October 2024 16:33:38

To mitigate the effect of the heat load, the diamond sample is mounted cantilever style to a thermally conductive SiC plate; and a 5 μs delay is placed between the laser initialization pulse and the microwave protocol used for NV measurements. Cantilever mounting also simplifies the subtraction of the birefringence background, since the only contribution comes from free space and rigidly aligned optics. Care must be taken to eliminate system drift, as it can blur together measurements of adjacent pixels. Our system does not exhibit significant drift over the course of measurements presented here, as evidenced by the high spatial resolution of imaged micrometer-scale defects in the sample, an example of which is presented in the supplementary material.

Figure 4 presents example images of the diamond sample's NV ensemble asymmetric resonance line shift in CW-ODMR (corresponding to the isometric stress component σ_{Diag} within the NV layer), T_2^*, T_1, and T_2; as well as optical birefringence over the full sample thickness, yielding both the relative stress magnitude and angle. Regions of stress typically correspond to NV spin resonance broadening and reduced T_2^*, limiting the sensitivity to magnetic fields in these locations (see additional information in the supplementary material).[14,15] T_2 is sensitive to the local nitrogen density in the diamond sample, which is homogeneous in the CVD diamond used here. If T_2^* is sufficiently poor in particular regions in the sample that a high-fidelity NV spin superposition state cannot be created with the Hahn echo protocol, then measurement of T_2 will include artifacts isolated to those poor T_2^* regions, which demonstrates the necessity of co-registered datasets for thorough characterization of the sample. We find that over 90% of the sample has measured T_2^* within 10% of the median value; and almost 99% of the sample has T_2 within 5% of the median T_2 value. Avoiding the few regions of enhanced stress and reduced T_2^* and T_2 is thereby enabled by all-in-on QDM characterization. Additional analysis, including a calculation of uncertainty values in the presented measurements, are presented in the supplementary material.

Figure 5 shows a specific region of enhanced stress at higher spatial resolution, selected from the QDM images of Fig. 4. In Fig. 5(a), the isometric stress component (σ_{Diag}) shows a region of increased stress that is between two linear regions in a channel ≈ 100 μm across. Stress petals, which are indicative of dislocation bundles that propagate from the substrate diamond during growth,[42,43] are visible nearby as much smaller features that are tens of micrometers across. Figure 5(b) shows that the two edges of the region of enhanced stress have related, but opposite, polarity shear components that extend across the region of increased σ_{Diag}. Figures 5(c) and 5(d) demonstrate that the out-of-plane shear components are localized only to the edges of the region of increased stress, and do not extend into the internal region. Figures 5(e) and 5(f) show that increased isometric stress is correlated with (and likely causal to) significantly reduced T_2^*, but with minimal effect on T_2. In particular, the edges of the stress region, which correspond to localized behavior in the shear components or to steep gradients in isometric stress, correlate with decreased T_2^* values. Figures 5(g) and 5(h) show stress magnitude and phase, respectively, determined from optical birefringence measurements, and provide quantitative confirmation of high stress regions determined from NV measurements.

V. CONCLUSION AND FUTURE WORK

We present a multi-functional quantum diamond microscope (QDM) for comprehensive characterization of NV-diamond samples. The apparatus employs automated components that enable remote operation. With modest future development, we envision push-button operation of all modalities described in this paper without user intervention. More significant future effort will likely be needed to extend the capability of this all-in-one QDM to remote operation on multiple samples in sequence, as a result of challenges with careful sample alignment, background subtraction with regard to birefringence, as well as good thermal heat-sinking.

The apparatus described in this paper should be extendable to any optically driven and detected solid-state quantum defect that operates at room temperature. There is a vast library of potential defects to be explored for optically driven quantum sensing, including vacancies and site defects,[44] transition metals,[45] and rare earth dopants[46,47] in both diamond and other semiconductor materials. The scale of characterization demands will continue to grow alongside developments in semiconductor defect systems, underlining the need for rapid characterization systems as described in this paper.

SUPPLEMENTARY MATERIAL

See the supplementary material for additional information about instrument design, function fitting, and GPU techniques to extract imaged parameters of interest, estimates of measurement uncertainty, and diamond sample surface cleaning and chemistry.

ACKNOWLEDGMENTS

The authors thank Brenda VanMil, Sean Blakley, and Matthew Trusheim for insightful conversations on solid state systems and NV physics. The authors also thank Adam Biacchi at NIST for implementing the conventional fume hood safe tri-acid diamond cleaning method used in this paper, as well as XPS analysis of the sample surface to confirm a successful cleaning and to interrogate surface chemistry. Support for this work was provided by the U.S. Army Research Laboratory, under Contract No. W911NF1920181, and the University of Maryland Quantum Technology Center.

AUTHOR DECLARATIONS

Conflict of Interest

Ronald L. Walsworth is a founder and advisor to companies that are developing and commercializing NV-diamond technology. These relationships are disclosed to and managed by the University of Maryland Conflict of Interest Office. The remaining authors have no conflicts of interest to disclose.

Author Contributions

Connor Roncaioli: Data curation (lead); Formal analysis (lead); Methodology (equal); Software (lead); Visualization (lead); Writing – original draft (lead). **Connor A. Hart:** Conceptualization (equal); Methodology (equal); Writing – review & editing (equal). **Ronald Walsworth:** Supervision (lead); Writing – review & editing (equal). **Donald Fahey:** Conceptualization (equal); Methodology (equal); Software (supporting); Writing – review & editing (equal).

DATA AVAILABILITY

The data that support the findings of this study are available from the corresponding author upon reasonable request.

25 October 2024 16:33:38

REFERENCES

[1]J. M. Taylor, P. Cappellaro, L. Childress, L. Jiang, D. Budker, P. R. Hemmer, A. Yacoby, R. Walsworth, and M. D. Lukin, Nat. Phys. **4**, 810 (2008).
[2]L. Rondin, J.-P. Tetienne, T. Hingant, J.-F. Roch, P. Maletinsky, and V. Jacques, Rep. Prog. Phys. **77**, 056503 (2014).
[3]E. R. Eisenach, J. F. Barry, M. F. O'Keeffe, J. M. Schloss, M. H. Steinecker, D. R. Englund, and D. A. Braje, Nat. Commun. **12**, 1357 (2021).
[4]I. Fescenko, A. Jarmola, I. Savukov, P. Kehayias, J. Smits, J. Damron, N. Ristoff, N. Mosavian, and V. M. Acosta, Phys. Rev. Res. **2**, 023394 (2020).
[5]F. Ziem, M. Garsi, H. Fedder, and J. Wrachtrup, Sci. Rep. **9**, 12166 (2019).
[6]N. Aslam, H. Zhou, E. K. Urbach, M. J. Turner, R. L. Walsworth, M. D. Lukin, and H. Park, Nat. Rev. Phys. **5**, 157 (2023).
[7]J. M. Schloss, J. F. Barry, M. J. Turner, and R. L. Walsworth, Phys. Rev. Appl. **10**, 034044 (2018).
[8]P. Wang, Z. Yuan, P. Huang, X. Rong, M. Wang, X. Xu, C. Duan, C. Ju, F. Shi *et al.*, Nat. Commun. **6**, 6631 (2015).
[9]J. S. Hodges, N. Y. Yao, D. Maclaurin, C. Rastogi, M. D. Lukin, and D. Englund, Phys. Rev. A **87**, 032118 (2013).
[10]M. E. Trusheim, K. Jacobs, J. E. Hoffman, D. P. Fahey, D. A. Braje, and D. Englund, "A polariton-stabilized spin clock," arXiv:2009.02427 (2020).
[11]T. Iwasaki, W. Naruki, K. Tahara, T. Makino, H. Kato, M. Ogura, D. Takeuchi, S. Yamasaki, and M. Hatano, ACS Nano **11**, 1238 (2017).
[12]S. C. Scholten, A. J. Healey, I. O. Robertson, G. J. Abrahams, D. A. Broadway, and J.-P. Tetienne, J. Appl. Phys. **130**, 150902 (2021).
[13]P. Neumann, I. Jakobi, F. Dolde, C. Burk, R. Reuter, G. Waldherr, J. Honert, T. Wolf, A. Brunner *et al.*, Nano Lett. **13**, 2738 (2013).
[14]P. Kehayias, M. J. Turner, R. Trubko, J. M. Schloss, C. A. Hart, M. Wesson, D. R. Glenn, and R. L. Walsworth, Phys. Rev. B **100**, 174103 (2019).
[15]A. Barfuss, M. Kasperczyk, J. Kölbl, and P. Maletinsky, Phys. Rev. B **99**, 174102 (2019).
[16]Y. Zhang, Q. Wu, H. Wu, X. Yang, S.-L. Su, C. Shan, and K. Mølmer, npj Quantum Inf. **8**, 125 (2022).
[17]D. P. Fahey, K. Jacobs, M. J. Turner, H. Choi, J. E. Hoffman, D. Englund, and M. E. Trusheim, Phys. Rev. Applied **20**, 014033 (2023).
[18]D. M. Toyli, D. J. Christle, A. Alkauskas, B. B. Buckley, C. G. V. de Walle, and D. D. Awschalom, Phys. Rev. X **2**, 031001 (2012).
[19]P. Bhattacharyya, W. Chen, X. Huang, S. Chatterjee, B. Huang, B. Kobrin, Y. Lyu, T. J. Smart, M. Block *et al.*, Nature **627**, 73 (2024).
[20]A. M. Edmonds, C. A. Hart, M. J. Turner, P.-O. Colard, J. M. Schloss, K. S. Olsson, R. Trubko, M. L. Markham, A. Rathmill *et al.*, Mater. Quantum Technol. **1**, 025001 (2021).
[21]E. V. Levine, M. J. Turner, P. Kehayias, C. A. Hart, N. Langellier, R. Trubko, D. R. Glenn, R. R. Fu, and R. L. Walsworth, Nanophotonics **8**, 1945 (2019).
[22]J. F. Barry, J. M. Schloss, E. Bauch, M. J. Turner, C. A. Hart, L. M. Pham, and R. L. Walsworth, Rev. Mod. Phys. **92**, 015004 (2020).
[23]F. Alghannam and P. Hemmer, Sci. Rep. **9**, 5870 (2019).
[24]C. Osterkamp, M. Mangold, J. Lang, P. Balasubramanian, T. Teraji, B. Naydenov, and F. Jelezko, Sci. Rep. **9**, 5786 (2019).
[25]B. K. Ofori-Okai, S. Pezzagna, K. Chang, M. Loretz, R. Schirhagl, Y. Tao, B. A. Moores, K. Groot-Berning, J. Meijer *et al.*, Phys. Rev. B **86**, 081406 (2012).
[26]M. C. Marshall, R. Ebadi, C. Hart, M. J. Turner, M. J. Ku, D. F. Phillips, and R. L. Walsworth, Phys. Rev. Appl. **17**, 024041 (2022).
[27]S. Knauer, J. P. Hadden, and J. G. Rarity, npj Quantum Inf. **6**, 50 (2020).
[28]E. R. Eisenach, J. F. Barry, L. M. Pham, R. G. Rojas, D. R. Englund, and D. A. Braje, Rev. Sci. Instrum. **89**, 094705 (2018).
[29]A. Przybylski, B. Thiel, J. Keller-Findeisen, B. Stock, and M. Bates, Sci. Rep. **7**, 15722 (2017).
[30]A. R. Lang, Nature **213**, 248 (1967).
[31]D. Howell, I. G. Wood, D. P. Dobson, A. P. Jones, L. Nasdala, and J. W. Harris, Contrib. Miner. Petrol. **160**, 705 (2010).
[32]D. Aude Craik, P. Kehayias, A. Greenspon, X. Zhang, M. Turner, J. Schloss, E. Bauch, C. Hart, E. Hu *et al.*, Phys. Rev. Appl. **14**, 014009 (2020).
[33]E. D. Herbschleb, H. Kato, Y. Maruyama, T. Danjo, T. Makino, S. Yamasaki, I. Ohki, K. Hayashi, H. Morishita *et al.*, Nat. Commun. **10**, 3766 (2019).
[34]S. Karaveli, O. Gaathon, A. Wolcott, R. Sakakibara, O. A. Shemesh, D. S. Peterka, E. S. Boyden, J. S. Owen, R. Yuste *et al.*, Proc. Natl. Acad. Sci. U. S. A. **113**, 3938 (2016).
[35]A. Savvin, A. Dormidonov, E. Smetanina, V. Mitrokhin, E. Lipatov, D. Genin, S. Potanin, A. Yelisseyev, and V. Vins, Nat. Commun. **12**, 7118 (2021).
[36]A. Lozovoi, H. Jayakumar, D. Daw, A. Lakra, and C. A. Meriles, Phys. Rev. Lett. **125**, 256602 (2020).
[37]A. Lozovoi, Y. Chen, G. Vizkelethy, E. Bielejec, J. Flick, M. W. Doherty, and C. A. Meriles, Nano Lett. **23**, 4495 (2023).
[38]N. Manson and J. Harrison, Diamond Related Mater. **14**, 1705 (2005).
[39]N. Aslam, G. Waldherr, P. Neumann, F. Jelezko, and J. Wrachtrup, New J. Phys. **15**, 013064 (2013).
[40]C. A. Hart, J. M. Schloss, M. J. Turner, P. J. Scheidegger, E. Bauch, and R. L. Walsworth, "N-v–diamond magnetic microscopy using a double quantum 4-ramsey protocol," Phys. Rev. Appl. **15**, 044020 (2021).
[41]K. J. Brown, E. Chartier, E. M. Sweet, D. A. Hopper, and L. C. Bassett, J. Chem. Health Saf. **26**, 40 (2019).
[42]H. Pinto and R. Jones, J. Phys.: Condens. Matter **21**, 364220 (2009).
[43]I. Friel, S. Clewes, H. Dhillon, N. Perkins, D. Twitchen, and G. Scarsbrook, Diamond Related Mater. **18**, 808 (2009).
[44]A. L. Falk, B. B. Buckley, G. Calusine, W. F. Koehl, V. V. Dobrovitski, A. Politi, C. A. Zorman, P. X.-L. Feng, and D. D. Awschalom, Nat. Commun. **4**, 1819 (2013).
[45]B. Diler, S. J. Whiteley, C. P. Anderson, G. Wolfowicz, M. E. Wesson, E. S. Bielejec, F. J. Heremans, and D. D. Awschalom, npj Quantum Inf. **6**, 11 (2020).
[46]G. Zhang, Y. Cheng, J. P. Chou, and A. Gali, Appl. Phys. Rev. **7**, 031308 (2020).
[47]L. Spindlberger, A. Csóré, G. Thiering, S. Putz, R. Karhu, J. U. Hassan, N. T. Son, T. Fromherz, A. Gali *et al.*, Phys. Rev. Appl. **12**, 014015 (2019).

25 October 2024 16:33:38